Scanning Microscopy

Volume 1990
Number 4 *Fundamental Electron and Ion Beam Interactions with Solids for Microscopy, Microanalysis, and Microlithography*

Article 16

1990

Slowing Down of Positrons and Applications to Solid Surfaces

Peter J. Schultz
The University of Western Ontario

L. R. Logan
The University of Western Ontario

W. N. Lennard
The University of Western Ontario

G. R. Massoumi
The University of Western Ontario

Scanning Microscopy Supplement 4, 1990 (Pages 223-237) 0892-953X/90$3.00+.00
Scanning Microscopy International, Chicago (AMF O'Hare), IL 60666 USA

SLOWING DOWN OF POSITRONS AND APPLICATIONS TO SOLID SURFACES

Peter J. Schultz*, L.R. Logan, W.N. Lennard and G.R. Massoumi

Department of Physics, The University of Western Ontario
London, Ontario, CANADA N6A 3K7

Abstract

When monoenergetic positrons enter a solid they scatter and lose energy via processes similar to those for electrons. Theoretical details of these processes have been well established for decades, but experimental results using low energy positron beams are only now becoming available for comparison. We review the theoretical results for elastic and inelastic scattering of positrons and the predictions that follow for backscattering, inner–shell ionization, energy loss and stopping profiles. In this presentation, emphasis is given to specific comparisons with calculations for electrons. We discuss recent experimental results in each of these areas, and conclude with two examples of applications of positron beam techniques to near–surface research.

KEYWORDS: positron slowing down, positron/electron comparisons, scattering cross sections, energy–loss, stopping, implantation profiles, surfaces, thin films, defect profiling

* Address for Correspondence:
Peter Schultz
Deptartment of Physics
The University of Western Ontario
London, Ontario, CANADA
N6A 3K7

PHONE: (519)661–3390
FAX: (519)661–2033
BITNET: pjs@uwovax

1.0 Introduction

Variable–energy positron beams have recently been receiving considerable attention due to the unique ways in which they can be used to study properties at and near solid surfaces (see, *e.g.*, Schultz and Lynn, 1988). The interaction of a monoenergetic positron (e^+) with a solid surface is in many ways different from that for the electron (e^-), which is precisely *why* its use as a solid–state probe is so interesting. In order to use positron–beam techniques for quantitative, analytical studies it is important to know where positrons stop in the solid, how they subsequently diffuse, and how they are affected by electronic and structural properties of the solid.

The processes involved in the slowing down of energetic positrons and electrons are similar. Incident particle directions are randomized through Mott (relativistic Coulomb) scattering, and the energy is lost via energy transfer to the bound electrons and by radiative processes (bremsstrahlung) (ICRU, 1984). The ratio of radiative to collisional energy loss is given by (Knoll, 1979)

$$\frac{(dT/ds)_r}{(dT/ds)_c} \cong \frac{TZ}{700} \qquad (1)$$

where T is the projectile kinetic energy in MeV and Z is the target atomic number. Energy loss down to a few hundred eV takes on the order of 10^{-12} s, independent of T. By this time the positron (*or* electron) will be very near its final position in the solid. The final stages of thermalization for a positron involve plasmon scattering (≈10–100 eV), electron–hole creation (≈0.1–10 eV), and phonon scattering (≈0–0.01 eV). Since these processes do not significantly affect the implantation profile shape, they will not be discussed further in this paper (Nieminen and Oliva, 1980).

The purpose of the present paper is to concentrate on the details of positron scattering, energy–loss, and eventual stopping in solids, which follows in §2 and §3. We develop the discussion around a review of previous theoretical work emphasizing the differences between positrons and electrons. We also include more recent experimental studies which systematically compare some of the interactions for monoenergetic positrons and electrons in the "low" energy region, ≈0–50 keV. To date, there are few data for these comparisons, but what does exist is leading to new questions as well as helping to establish the necessary stopping profiles. The

Table of Symbols

b	–impact parameter [Eq. (6)]
c	–speed of light
D	–surface dipole potential [Eq. (14)]
e	–electron charge
$\hbar$	–Planck's constant
I	–mean ionization energy [Eq. (7)]
m	–electron mass
N	–atom density
P	–positron stopping profile [Eq. (10)]
q	–kinetic energy loss
r_0	–classical electron radius (e^2/mc^2)
s	–Doppler broadening parameter [Fig. 24]
Δs	–path length [Eq. (9)]
Δt	–collision time [Eq. (6)]
T	–projectile kinetic energy
$\Delta\hat{T}$	–most probable energy loss [Fig. 17]
U	–ionization energy for inner shell electron
v	–projectile velocity
z	–depth in the solid [Eq. (10)]
Z	–atomic number
α	–fine structure constant ($e^2/\hbar c$)
β	–v/c
γ	$-(1-\beta^2)^{-1/2}$
ϵ	–fractional energy transfer (q/T)
ϵ_m	–maximum fractional energy transfer
η^+	–positron backscattering coefficient [Fig. 6]
η^-	–electron backscattering coefficient [Fig. 4]
θ	–scattering angle [Eq. (2)]
$<\theta>$	–mean (positive) scattering angle [Fig. 2]
μ^+	–positron chemical potential [Eq. (14)]
μ^-	–electron chemical potential [Eq. (14)]
σ^+	–elastic scattering cross section for positrons
σ^-	–elastic scattering cross section for electrons
σ_M	–Møller scattering cross section [Eq. (4)]
σ_B	–Bhabha scattering cross section [Eq. (5)]
τ	–electron orbit time for inner shell [Eq. (6)]
χ	$-(2\pi e^4)/(mv^2)$ [Eq. (4)]
Ω	–solid angle
Ω^2	–energy loss straggling [Eq. (9)]

comparative e^-/e^+ experiments are also of fundamental interest, since the electron–positron is the simplest matter–antimatter system which can be studied in the laboratory. Accurate measurements will be useful for guiding calculations, which are usually approximate and often intractable at these low energies.

Following our discussion of positron stopping, we conclude in §4 with a brief discussion of two applications of the positron–beam technique: (i) positron re–emission studies of thin metal films, and (ii) defect profiling in semiconductor epilayers grown by molecular beam epitaxy (MBE).

2.0 Elastic Scattering

Exact elastic scattering cross sections for both electrons (σ^-) and positrons (σ^+) from the central coulomb field of an ion core (charge Ze) were given in the form of a series of Legendre polynomials by Mott (1929; 1932). These were subsequently approximated by several authors by a Born series expansion in aZ ($a=e^2/\hbar c$) (see, *e.g.*, Rohrlich and Carlson, 1954). The second Born approximation for the differential cross sections with respect to the scattering angle θ are

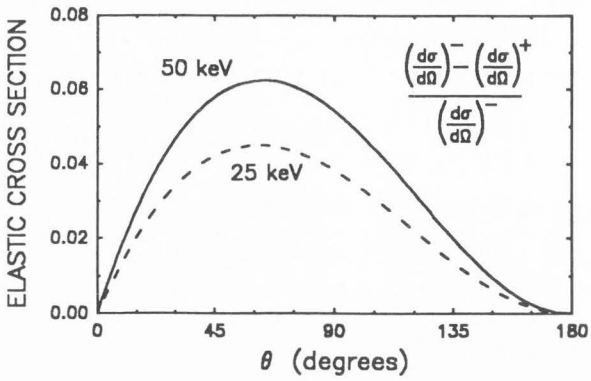

Figure 1: Relative difference of elastic scattering cross sections for electrons and positrons as a function of scattering angle, θ. Data are calculated using Eq. (2) for T=25 keV ($\gamma\approx1.05$) and T=50 keV ($\gamma\approx1.10$), and an aluminum target.

$$\left(\frac{d\sigma}{d\Omega}\right)^{\pm} = \left(\frac{r_0 Z}{2\beta^2\gamma\ \sin^2(\theta/2)}\right)^2 \times \Big(1 - \beta^2\sin^2(\theta/2) \mp aZ\pi\beta(\sin(\theta/2)[1-\sin(\theta/2)])\Big) \qquad (2)$$

where $\beta=v/c$, $\gamma=(1-\beta^2)^{-1/2}$, and $r_0=e^2/mc^2$. Eq. (2) shows that $(d\sigma^-/d\Omega)$ is generally larger than $(d\sigma^+/d\Omega)$, for reasons discussed below. For *non*relativistic e^- and e^+ it is often sufficient to use a simple (screened) Rutherford cross section for elastic scattering which, contrary to Eq. (2), is independent of the sign of the charge (Bishop, 1967). At *very* low energies (*i.e.*, below a few keV), the Rutherford cross section is no longer valid because of atomic effects, and elastic scattering cross sections are again significantly different for electrons and positrons. In this case the difference arises due to the increased importance of electrons in the scattering potential (as the incident projectile wavelength gets larger), which contributes an exchange term for incident electrons (but *not* for positrons). Calculations in this energy regime have been presented by Valkealahti and Nieminen (1984).

The Mott scattering expansion in Eq. (2) is a good approximation for light elements, although the characteristics are generally true for all Z. The second order term of Eq. 2 (*i.e.* the term cubic in Z) is required because of the quantum mechanical nature of the interaction (since both e^- and e^+ are spin 1/2 fermions) (Evans, 1955). The positron–electron difference arises because this term (*i.e.* as with all higher even terms in the (aZ) expansion) is proportional to an odd power of Z, and therefore dependent on projectile charge. This difference can be several percent for projectile energies of T=25 keV ($\gamma\approx1.05$) and T=50 keV ($\gamma\approx1.10$), as shown for an aluminum target in Fig. 1. The differences tend to be largest at intermediate angles, although these events are relatively rare. Nevertheless, it is primarily those medium to large angle scattering events which lead to the distribution of backscattered positrons or electrons (discussed in the next section). The more frequent small angle scattering events lead to a broadening of the incident beam direction. Such small–angle multiple scattering effects have been calculated by Sigmund and Winterbon (1974) and by Lindhard (1965).

As electrons or positrons traverse a solid, they lose energy and continue to scatter elastically. Using the

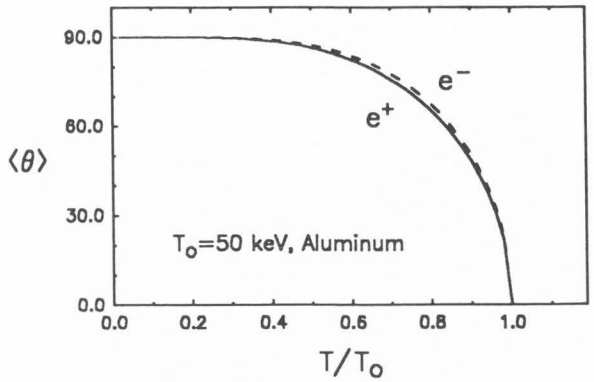

Figure 2: Average total scattering angle, $<\theta>$, versus instantaneous energy, T/T_0, for 50 keV electrons and positrons slowing down in aluminum.

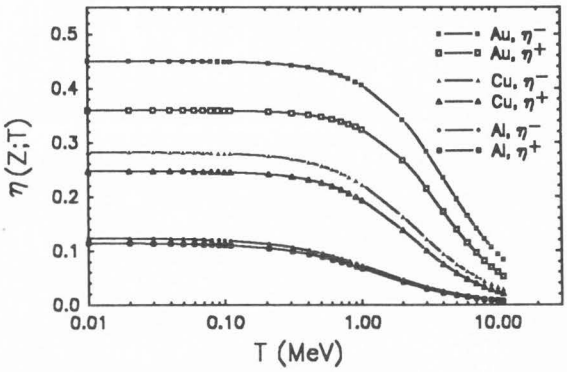

Figure 3: Backscattering coefficients, η, calculated for electrons and positrons versus incident energy T and atomic number Z (calculated following Kuzminikh et al., 1974).

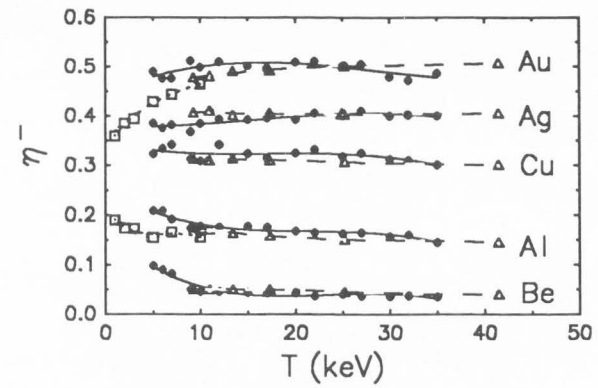

Figure 4: Experimental data for electron backscattering coefficient, η^-, versus incident energy T for several different materials. Solid circles are preliminary data from our laboratory, open triangles are from Drescher et al. (1970), and open squares are Monte Carlo calculations from Valkealahti and Nieminen (1984).

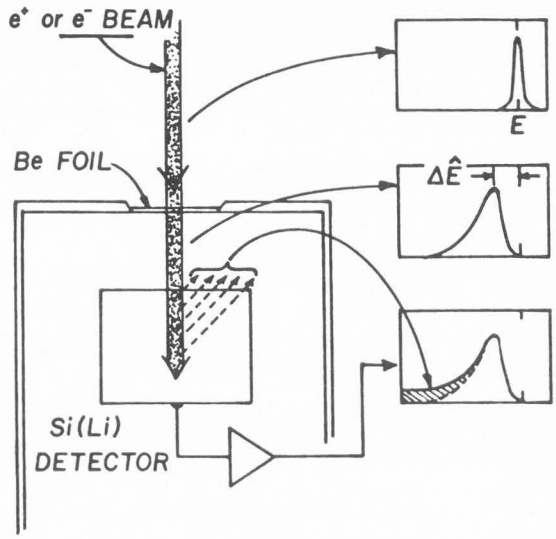

Figure 5: Experimental geometry for measuring energy–loss distributions for electrons and positrons through ≈1.5 mg/cm² Be foil. The hatched portion of the distribution is attributed to backscattering from the Si detector. The values deduced for η^- and η^+ at ≈45 keV were the same (to within ≈1%), contrary to the prediction of ≈10% difference that is suggested by the data in Fig. 3 (after Lennard et al., 1988a).

continuous slowing down approximation (see, *e.g.*, ICRU, 1984) and following Rohrlich and Carlson (1954), we show the average multiple scattering angle $<\theta>$ as a function of the instantaneous energy in Fig. 2 for electrons and positrons incident on aluminum (T_0=50 keV). The dramatic angular spread is a consequence of the full scattering cross section, Eq. (2).

2.1 Backscattering

Large angle elastic (single) scattering, or plural scattering at intermediate angles, ultimately leads to some fraction of the incident beam being backscattered from the solid. The backscattered fraction, η, is a function of material (Z, density and thickness) and of incident particle energy. A relatively small fraction are backscattered elastically, since by the time the particles escape through the surface of the sample they have generally traversed (at least) several hundred angstroms of material. Differences in the elastic cross sections result in significantly different predictions for η^- (e^-) and η^+ (e^+). As shown previously in Fig. 1, this suggests that $\eta^->\eta^+$ for *all* energies regardless of whether the backscattered event was caused by only a few large angle collisions, or several small angle collisions. The dependence of backscattering on projectile type, energy, and material is illustrated in Fig. 3, which is based on the semi–empirical formulae of Kuzminikh et al. (1974). A great deal of experimental evidence for electron backscattering has confirmed the shape and (in most cases) the magnitude of the predictions in the figure (see, *e.g.*, Tabata and Okabe, 1971, and Kuzminikh et al., 1974). We note at this time that our calculations for aluminum shown in Fig. 3 do *not* agree with those shown in the original reference. Our calculations are in agreement for all other materials, and we conclude that Fig. 1 in Kuzminikh et al. (1974) is in error.

In the low energy range of present interest experimental data is sparse, as shown in Fig. 4. The results shown here for η^- are taken from Drescher et al. (1970), and compared with relatively recent Monte Carlo calculations (Valkealahti and Nieminen, 1984) and our own preliminary results. Other studies of electron

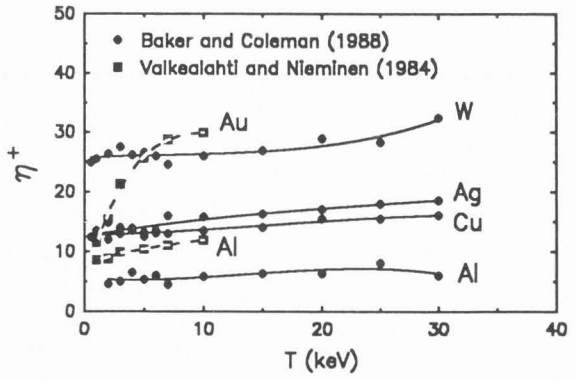

Figure 6: Experimental data for positron backscattering coefficient, η^+, versus incident energy, T.

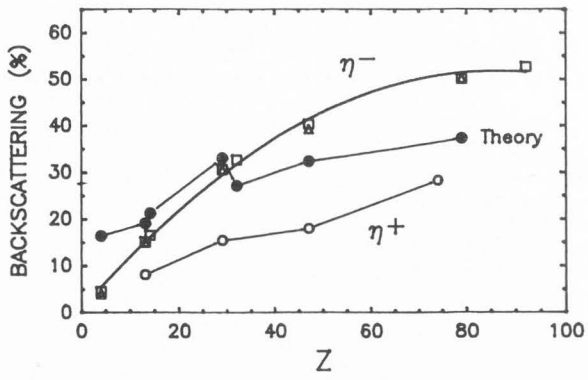

Figure 7: Backscattering coefficients versus atomic number Z for electrons and positrons with T=25 keV. Open circles are data of Baker and Coleman (1988), and open squares are from Drescher et al. (1970). Open triangles are data from our laboratory, and the "Theory" (solid circles) is a simple quantum mechanical calculation based on plane waves incident on an appropriately scaled Kronig–Penny (box) potential.

backscattering, which address target thickness and backscattered energy and angular distributions, as well as incident energy dependence, are presented by Cosslett and Thomas (1965), Vyatskin and Trunev (1967), Matsukawa et al. (1974), Darlington (1975), and Hunger and Rogaschewski (1986).

There are even fewer experimental results for *monoenergetic* positrons than for electrons. One indirect measurement of an η^- to η^+ comparison for silicon was reported by Lennard et al. (1988a). The experiment, shown schematically in Fig. 5, was to study e^- and e^+ energy–loss distributions through a thin Be target (results discussed in §3.2). Indicated on the figure is the part of the distribution measured with a Si(Li) detector that is due to the incomplete energy deposition of backscattered particles (hatched). In this study we found *no* measurable difference (to within 1%) between η^- and η^+ in Si at ≈45 keV, which does not agree with the theoretical predictions that η^- should be at least 10% larger than η^+ (Fig. 3). More direct measurements of positron backscattering have been made by Baker and Coleman (1988), which are shown together with Valkealahti and Nieminen's (1984) Monte Carlo predictions. These data are shown in Fig. 6, and by comparison with the results in Fig. 4 they support the theoretical prediction that $\eta^+<\eta^-$ for any given material. Ongoing experimental studies at our laboratory will, hopefully, complement these data in the near future.

Most information available on backscattering (both theoretical and experimental) suggests that there is a monotonic dependence of η on *both* film thickness and atomic number (see, *e.g.*, Cosslett and Thomas, 1965, and Darlington, 1975). In one theoretical investigation designed expressly to study the Z–dependence, Logan et al. (1988) used a simple Kronig–Penney model potential which was modified to include the solid surface. Here, the electron and positron Schrödinger equation could be solved exactly. Their results, shown by the solid line in Fig. 7, illustrate that the Z–dependence of the atomic density translates directly to a prediction of structure in the backscattered fractions. Some of the structure predicted by this model is supported by the experimental measurements of η^+ by Baker and Coleman (1988), also shown in Fig. 7.

In spite of decades of research (*particularly* for electrons), experimental backscattering data are not sufficiently precise *or* consistent to allow a credible comparison with theory. The study of electron and positron backscattering differences will continue to be an active area of research.

3.0 Inelastic Scattering

Scattering of electrons of kinetic energy T by *free electrons* is described by Møller's (1932) cross section,

$$\left(\frac{d\sigma_M}{d\epsilon}\right) = \frac{\chi}{T}\left(\frac{1}{\epsilon^2}+\frac{1}{(1-\epsilon)^2}+\left[\frac{\gamma-1}{\gamma}\right]^2-\frac{(2\gamma-1)}{\gamma^2}\times\frac{1}{\epsilon(1-\epsilon)}\right) \quad (3)$$

$$\chi = \frac{2\pi e^4}{mv^2} = \frac{2\pi r_0^2 mc^2}{\beta^2}; \quad r_0 = \frac{e^2}{mc^2} \quad (4)$$

In the above ϵ is the fractional energy transfer, q/T, and the total energy of the incident electron is $E=\gamma mc^2=T+mc^2$. Because of the indistinguishability of electrons, the outgoing electron with the higher energy in a binary collision is defined as the primary electron. For this reason, the maximum energy transfer possible in Møller scattering is $\epsilon_m=1/2$.

For positrons the appropriate relativistic cross section for energy transfer to a free electron was derived by Bhabha (1936),

$$\left(\frac{d\sigma_B}{d\epsilon}\right) = \frac{\chi}{T}\left\{\frac{1}{\epsilon^2}-\frac{\gamma^2-1}{\gamma^2\epsilon}+\frac{1}{2}\left[\frac{\gamma-1}{\gamma}\right]^2 - \left[\frac{\gamma-1}{\gamma+1}\right]\times\left[\frac{\gamma+2}{\gamma\epsilon}-\frac{2\gamma^2-2}{\gamma^2}+\epsilon\left[\frac{\gamma-1}{\gamma}\right]^2\right] + \left[\frac{\gamma-1}{\gamma+1}\right]^2\times\left[\frac{1}{2}+\frac{1}{\gamma}+\frac{3}{2\gamma^2}-\epsilon(1-\epsilon)\left[\frac{\gamma-1}{\gamma}\right]^2\right]\right\} \quad (5)$$

Following Rohrlich and Carlson (1954), we illustrate the difference between Møller and Bhabha cross sections in Fig. 8 by plotting their ratios to the common prefactor $\chi/T\epsilon^2$, for both T=25 keV and T=50 keV. Inelastic scattering at these energies is much stronger for positrons than for electrons due to the larger differential cross section and to the absence of a cutoff at $\epsilon_m=1/2$. These effects lead to larger energy straggling and mean energy loss for positrons than for electrons.

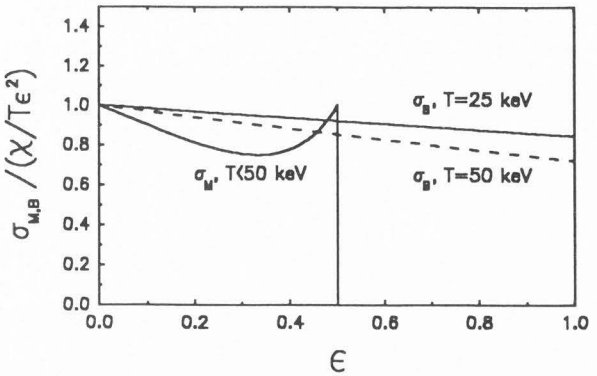

Figure 8: Differential inelastic cross sections for electron–electron (Møller, σ_M) scattering and positron–electron (Bhabha, σ_B) scattering. Cross sections are shown for T=25 and 50 keV, relative to the common prefactor in Eqs. (3) and (5), $\chi/T\epsilon^2$, where χ is given in Eq. (4) and ϵ is the fractional energy transfer in a collision.

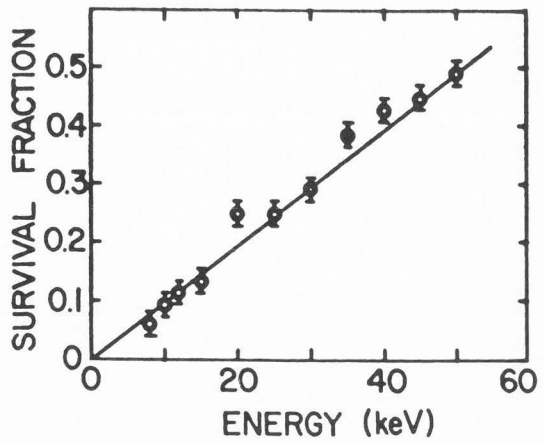

Figure 9: Survival fraction for 50 keV incident positrons channeling through the <100> axis of a 2600 Å (≈60 μg/cm^2) silicon single crystal. The figure clearly indicates that *even* at keV energies, a significant fraction of the incident positrons pass through the crystal without being dechanneled (after Schultz et al., 1988a).

One effect that is often neglected in calculations of energy loss and inelastic scattering is channeling (Lindhard, 1965). Channeling is the phenomenon whereby energetic particles are guided by the nearly continuous potential of a highly ordered crystalline solid. The assumption that channeling effects are *not* important is reasonable for electrons, which interact too strongly with the ion cores at these low energies (<100 keV). In contrast to this, positrons have been shown to have a relatively high probablility of channeling in this energy region (Schultz et al., 1988a). This is illustrated in Fig. 9, where the fraction of the incident beam that is *still* channeled after transmission through a 2600 Å (≈60 μg/cm^2) Si(100) crystal is shown to be a linear function of incident energy. For stopping distributions of positrons, channeling must be considered as potentially important either directly upon entering a crystalline target (*i.e.*, the *usual* channeling process) or else by "feeding in" to high–symmetry directions during the slowing down and scattering process.

3.1 Inner–shell ionization

One of the clearest examples of the difference between Møller and Bhabha scattering which has been observed experimentally is for inner–shell ionization. These events involve the largest energy transfers in the slowing down process, although they tend to be rare and therefore less important in stopping than the more numerous outer shell (or soft) collisions.

In Fig. 10 we show results for L–shell ionization of a thin (40 μg/cm^2) Au target using monoenergetic electrons and positrons between 25 and 55 keV (Lennard et al., 1988b). The data are plotted as the ratio of the total cross sections, and show the first directly measured evidence that the Bhabha cross section is greater than the Møller cross section at these energies. Kolbenstvedt (1967) developed a theory for estimating K–shell ionization by electrons which separated the contributions for impact parameters greater than and less than the shell radius. The large impact parameter projectiles contribute to the total ionization only through the electric field, which is equivalent to a radiation field in the limit $\beta \to 1$. The close collision effects are estimated by integrating the Møller cross section over all energy transfers from the mean ionization potential, $\epsilon = U/T$, to

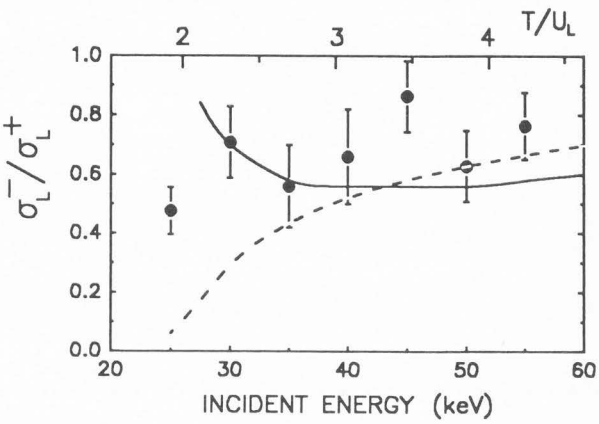

Figure 10: Au L–shell ionization cross section for electrons (σ_L^-) normalized to that for positrons (σ_L^+). These data show the first evidence of the dominant Bhabha scattering cross section, since the ratio is consistently less than unity. The theoretical curves are described briefly in the text (Lennard et al., 1988b).

$\epsilon_m = 1/2$ (where U is the ionization potential). This calculation was extended to positron ionization using the Bhabha cross section, where $\epsilon_m = 1$, and applied to the L–shell in order to obtain the predicted cross section ratio shown by the dashed line in Fig. 10.

It is important to note that both Møller and Bhabha cross sections describe *free* particle collisions, and they are clearly *not* applicable if the orbit time of the bound electron is comparable to the interaction time. Assuming that the collision time is approximately the time duration of the electromagnetic impulse as the projectile passes the atom, $\Delta t \approx b/\gamma v$ (b=impact parameter), we estimate the ratio of collision time to orbit period, τ, to be

$$\frac{\Delta t}{\tau} \approx \frac{bU}{2\pi\hbar c\gamma\beta} \qquad (6)$$

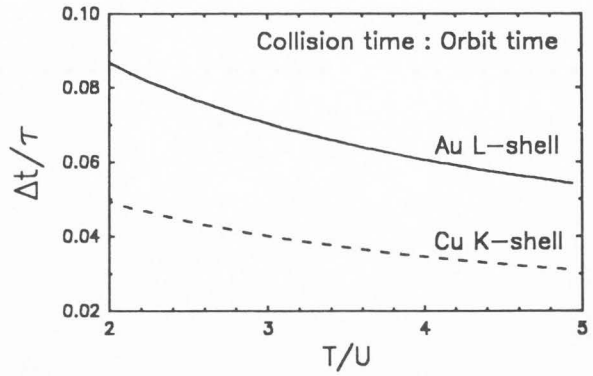

Figure 11: Ratio of collision time (Δt) to orbit time (τ) for K–shell collisions in Cu and L–shell collisions in Au. The small ratio, taken from Eq. (6) in the text, supports the application of free–particle Møller and Bhabha cross sections in the calculation of inner shell ionization probabilities.

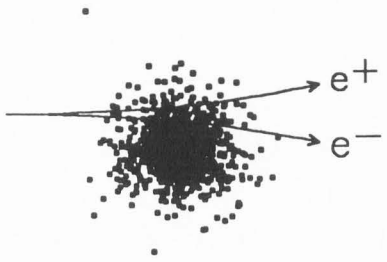

Figure 12: Schematic to illustrate the semiclassical inner–shell ionization calculation. Classical trajectories are used to calculate the projectile wavefunction overlap with atomic electron wavefunctions, shown above for the radially symmetric Cu K–shell. The incident electron overlap is larger than that for the positron due to the Coulomb field of the nucleus. Also, the electron velocity is increased while the positron velocity is decreased. Both of these effects lead to corrections which *increase* the cross section for inner shell ionization by electrons, and *decrease* the cross section for positrons.

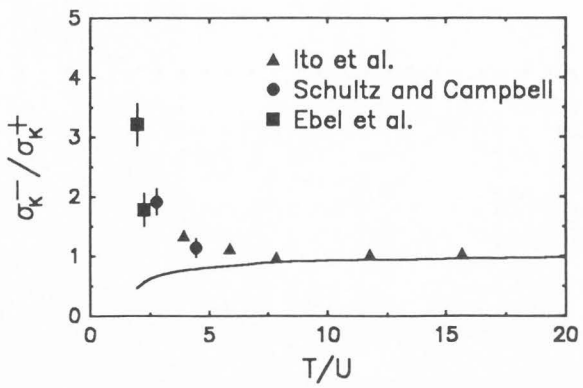

Figure 13: K–shell ionization cross section for electrons (σ_K^-) normalized to that for positrons (σ_K^+). Data shown are for Cu (Schultz and Campbell, 1985; Ebel et al., 1988) and Ag (Ito et al., 1980). The solid line is calculated using the uncorrected free particle cross sections. The strong Coulomb correction is demonstrated by the fact that the ratio is *never* less than unity.

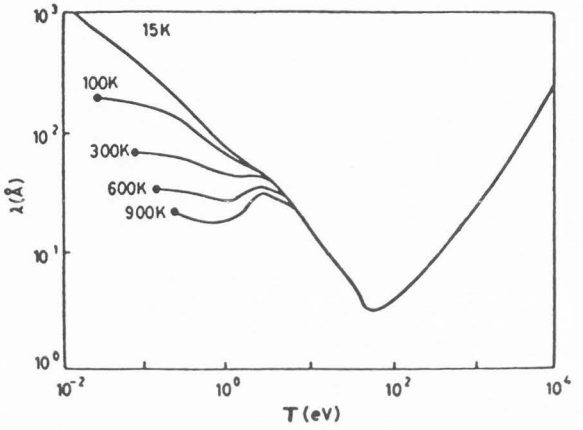

Figure 14: Inelastic mean free path λ for positrons at energy T in an Al sample at different temperatures (after Nieminen and Oliva, 1980).

Fig. 11 shows this ratio for the L–shell of Au (U≈12.98 keV) and the K–shell of Cu (U≈8.98 keV) as functions of energy (T/U). Within the context of the very crude estimate represented by Eq. (6), it can be seen that the application of the "free" particle cross sections are not unreasonable.

A significant difficulty with the calculation lies in the fact that one of the electrons is bound. This means that it is possible to observe an event originating from a "close" collision for which ϵ>1/2, by the characteristic X–ray which follows the ionization. Such events cannot be included in an integral over the Møller's free electron cross section, since electron indistinguishability is inherent in Møller's derivation. The appropriate close collision cross section for the ionization process must therefore be derived from first principles. It is also significant that most of the problems with inner–shell ionization calculations occur at the lower energies (T/U≈2–3). In this extreme the distant collision contribution can be as much as 50% or more of the total cross–section, even though its calculation has so far been based on fairly broad assumptions.

The most obvious source of discrepancy between the Kolbensvedt type of theory and the data shown in Fig. 10 is the distortion of the incoming projectiles due to the Coulomb field of the nucleus. Fig. 12 shows a schematic representation of both e^- and e^+ trajectories through the electron cloud of an atom, from which two significant "Coulomb" effects can be inferred. First, the average electron separation from the nucleus will be less than that for positrons, which will increase the overlap of the incident projectile with the atomic electron and therefore *increase* σ^- relative to σ^+. Secondly, and more important, the electron will speed up as it approaches the nucleus, whereas the positron will slow down. Several authors have derived semiempirical expressions for total ionization cross sections, one of the more popular being Gryzinski's (1965) (see Powell, 1976, for a review). At low velocities these all show a strongly positive dependence on energy, and thus the velocity shift should *also* increase σ^- relative to σ^+. This effect was included in the theoretical calculation of the L–shell ionization cross–section ratio given by the solid line in Fig. 10 (Lennard et al., 1988b). The method involves the calculation of an ionization probability over a set of classically determined electron trajectories. The local

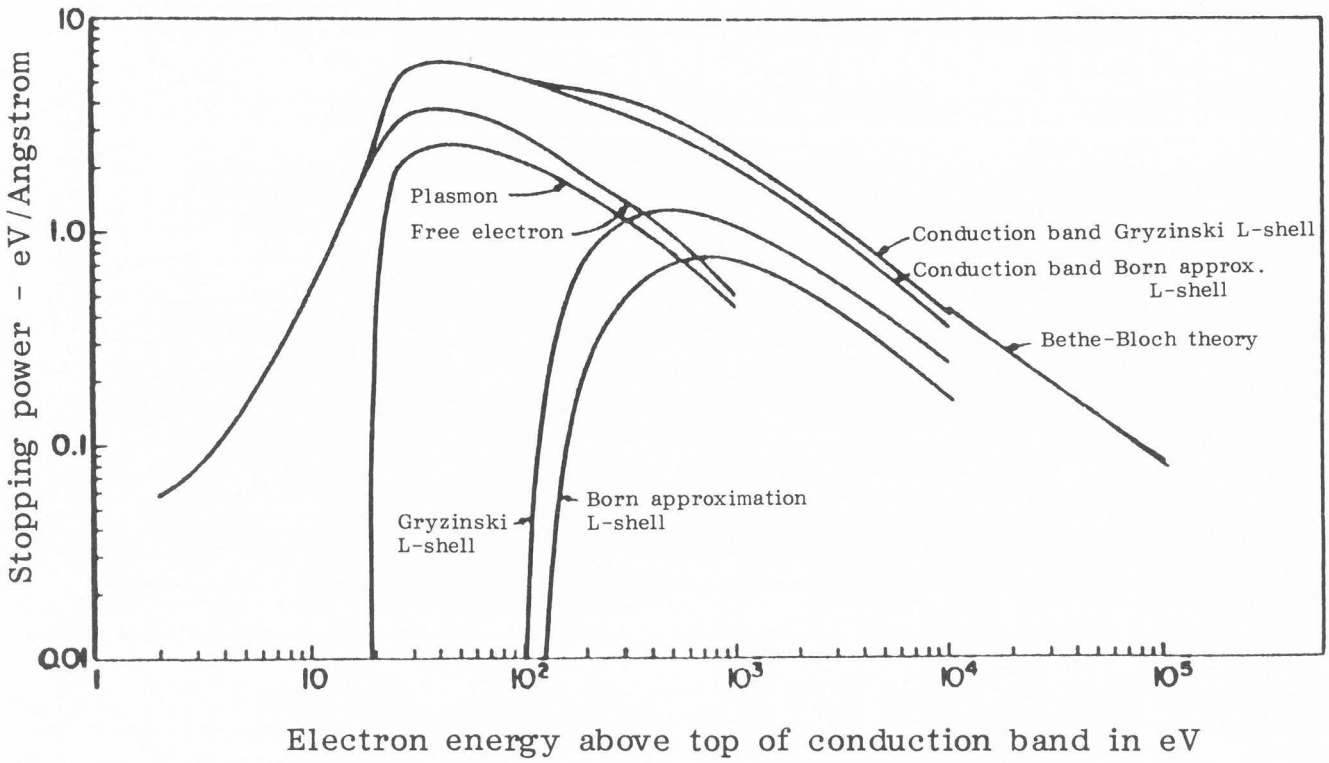

Figure 15: Stopping power versus electron energy in Al. The relative contributions of different scattering processes are separated, showing the dominance of ionization processes at energies above a few hundred eV. The "universal" scattering curve in Fig. 14 is scaled from the inverse of this figure. (After Ashley et al., 1979)

ionization probability along such a path is weighted by the atomic electron probability density function, $|\psi(\underline{r})|^2$. The contribution to the total ionization cross section due to close collisions is then obtained by summing over all classical paths in three dimensions. The contribution to the cross section from distant collisions ($b \geq a$) is approximated using the Weizsäcker–Williams method of virtual quanta (see, *e.g.*, Jackson, 1975). More realistic dynamic limits for the separation between distant and close collisions were also considered in the model. The solid curve in Fig. 10 shows the model, which predicts the Au L–shell data reasonably well.

Electron/positron comparisons have been made for K–shell ionization of Ag by Ito et al. (1980), and for Cu by Schultz and Campbell (1985) and Ebel et al.(1988). These data are shown in Fig. 13 together with the Kolbenstvedt–type prediction (solid line). The influence of the Coulomb field of the nucleus on the relative ionization cross sections is much more pronounced for the K–shell. The theoretical calculations are much less successful in reproducing the measurements than they were for the L–shell data of Fig. 10.

3.2 Energy loss

The collisional stopping power, due to energy transfer from incident projectiles to bound atomic electrons, is characterized by the cross sections responsible for these processes (Tougaard and Sigmund, 1982). The mean free path for inelastic collisions, λ, has been discussed for electrons by several authors (see for example references 28–30), and for positrons by Nieminen and Oliva (1980). The latter result for λ as a function of temperature and energy is shown for Al in Fig. 14. The figure illustrates the "universal" curve that is observed for all materials and (with a slight scale shift) for both positrons and electrons. The contribution of different processes is shown in Fig. 15, in this case for the stopping power as a function of energy for electrons in Al (Ashley et al., 1979). Above ≈1 keV it can be seen that free electron and plasmon excitations are not important, and that the higher cross section for conduction electron scattering makes it at least as important as the inner–shell collisions, in spite of the lower energy transfer per collision.

The calculation of energy loss is derived from the Bethe–Bloch formalism (Bethe, 1933), which separates energy transfers into two classes depending on whether ϵ is above or below a limiting value, $\epsilon_1 = q_1/T$. This was discussed by Rohrlich and Carlson (1954) and by Uehling (1954), as well as in the ICRU tables (1984), and our account is drawn from those sources. A related discussion of energy loss for low energy electrons is given by Bichsel (1990). The limit, q_1, is chosen to meet two criteria. The first is that q_1 is large compared to the (outer shell) atomic electron binding energies of the stopping medium, and the second is that impact parameters associated with small energy transfer collisions ($\epsilon < \epsilon_1$) are large compared to atomic dimensions. The *average* energy loss per unit path length, or stopping power, for small energy transfers is derived using the Bethe–Bloch collision cross–section, with the result

$$\left[\frac{-dE}{ds}\right](\epsilon<\epsilon_1) = NZ\chi\left[\ell n\left[\frac{2T^2\epsilon_1(\gamma+1)}{I^2}\right]-\beta^2\right] \qquad (7)$$

where N is the atom density, and I is an average

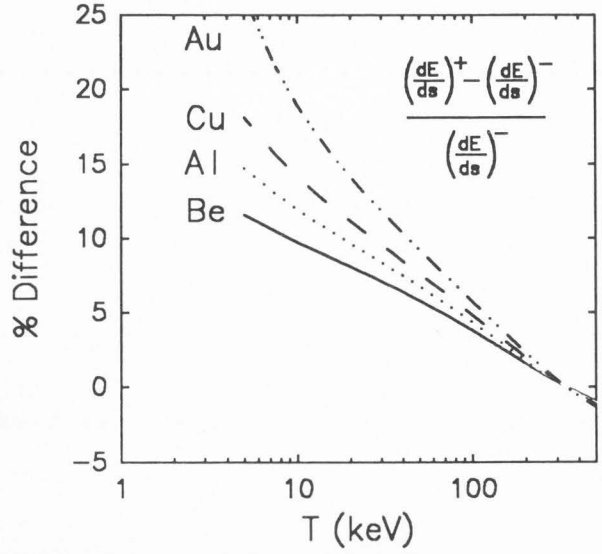

Figure 16: Percent difference in mean energy loss for positrons minus electrons in several different solids. The cross–over reflects the fact that the Bhabha cross section is on average greater than the Møller cross section below ≈345 keV, whereas the reverse is true at higher energies.

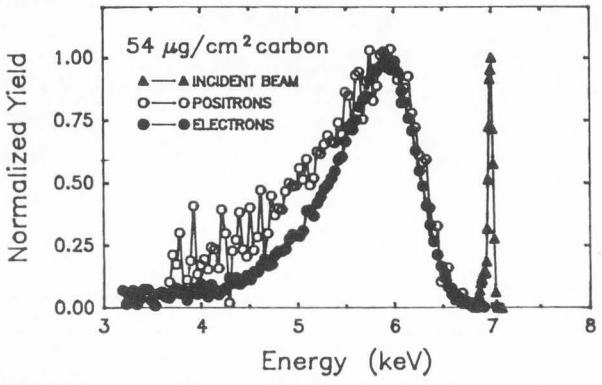

Figure 18: Energy loss distributions for 7 keV electrons (solid circles) and positrons (open circles) incident on ≈54 μg/cm² carbon. The incident projectiles are monoenergetic, and the narrow distribution (solid triangles) reflects the resolution of the retarding–field energy analyzer. As predicted, the most probable energy loss is similar for both e^- and e^+. Significantly different widths of the distributions would also be predicted (see Fig. 16).

ionization potential.

For collisions involving large energy transfers the atomic electrons are regarded as free and at rest, and the appropriate differential inelastic cross–section is integrated over all possible energy transfers to obtain the stopping power

$$\left[\frac{-dE}{ds}\right]^{\pm}(\epsilon>\epsilon_1) = NZT\int_{\epsilon_1}^{\epsilon_m}\epsilon\, d\sigma$$

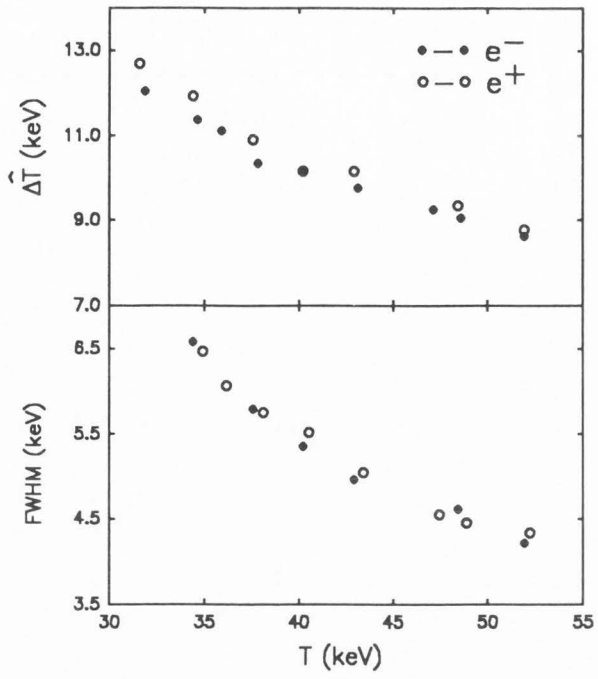

Figure 17: Most probable energy, $\hat{\Delta T}$, and full width at half maximum, FWHM, are shown for the energy loss distributions of electrons (solid circles) and positrons (open circles) after traversing a ≈1.5 mg/cm² Be target. Data support the theoretical estimates that differences would be insignificant for $\hat{\Delta T}$, and would be *less* than 2% for FWHM (after Lennard et al., 1988a).

$$= NZT\int_{\epsilon_1}^{\epsilon_m}\epsilon\left[\frac{d\sigma}{d\epsilon}\right]d\epsilon \qquad (8)$$

The upper limit of the integral is ϵ_m=1/2 if the calculation is for electrons (Møller's cross–section, Eq. (3)), or ϵ_m=1 for positrons (Bhabha's cross–section, Eq. (5)).

The total stopping power is the sum of Eqs. (7) and (8), which is larger for positrons than for electrons by ≈6–10% in the low energy region of present interest. This is reflected in Fig. 16, where we show the relative difference for positrons and electrons (Rohrlich and Carlson, 1954). The crossover at ≈345 keV in Fig. 16 is due to the fact that the Møller cross section becomes larger than the Bhabha cross section at high energies. The ICRU (1984) have compiled extensive tables for stopping power versus energy for both positrons and electrons in various materials.

Experimental studies of stopping are normally done by measuring the energy distribution of particles transmitted through foils that are thin compared to the particle range. This distribution is characterized by a peak corresponding to the most probable energy loss, $\hat{\Delta T}$, and a tail extending to lower energy. In discussing energy loss distributions, the individual collisions are usually classified as soft, intermediate or hard, depending on whether the energy transfer involved is less than, near to, or greater than a critical value, ϵ_c (ϵ_c≈0.005, *i.e.*, energy transfer ≈0.005T). The soft and intermediate collisions determine the most probable energy loss, $\hat{\Delta T}$,

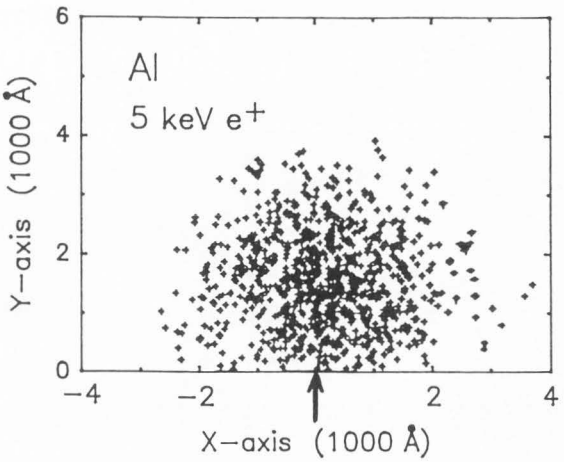

Figure 19: Monte Carlo calculation of 5 keV incident positrons stopping in aluminum (from Valkealahti and Nieminen, 1984).

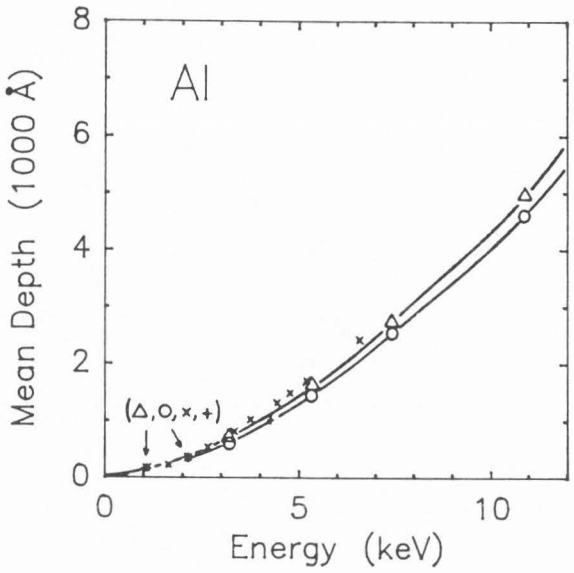

Figure 20: Mean stopping depth for positrons (open triangles) and electrons (open circles) calculated by Monte Carlo simulation as in Fig. 19 (Valkealahti and Nieminen, 1984). Also shown are experimental data for positrons (cross, Mills and Wilson, 1982) and for electrons (plus, Vyatskin and Khramov, 1976).

since the hard collisions are so improbable. Thus, the different maximum energy transfers (ϵ_m) for electrons and positrons have little influence on $\Delta\hat{T}$. This has been demonstrated experimentally for 38–56 keV electrons and positrons passing through a 1.5 mg/cm² Be foil, as shown in Fig. 17 (Lennard et al., 1988a). This is also illustrated for much lower energy (7 keV) electrons and positrons in Fig. 18. The latter data were obtained using a magnetically guided positron beam (Schultz, 1988) and a retarding–field analysis of the transmitted particle energy. The near equivalence of $\Delta\hat{T}$ for electrons and positrons in both figures 17 and 18 is apparent.

The high loss part of the distribution is caused primarily by the hard collisions, and the full width at half maximum (FWHM) is determined primarily by the intermediate collisions. Differences in the *shapes* of the energy loss distributions for $\Delta T > \Delta\hat{T}$ are, therefore, related to differences in the corresponding Møller and Bhabha cross sections for energy transfers *near* $\epsilon = \epsilon_c$. These differences are amplified in the FWHM due to the dependence of energy loss straggling, Ω^2, on the *square* of the energy transfer as opposed to the linear dependence for stopping power (Eq. (8)), viz,

$$\Omega^2 = NZT^2\Delta s \int \epsilon^2 d\sigma \qquad (9)$$

where Δs is the path length. The experimentally determined FWHM's of the energy loss distributions for equivelocity electrons and positrons between 38 and 56 keV are shown in Fig. 17. For this case, we expect little difference based on Landau's (1944) prediction, as discussed by Lennard et al. (1988a). However, for the 7 keV incident particles shown in Fig. 18, Landau's prescription would lead us to predict ≈5% larger FWHM for positrons than for electrons. We observe an even larger effect in these preliminary data, for which we have no explanation at this time. More precise and systematic experiments designed to address these questions at low energies are presently underway.

3.3 Stopping profiles

Experimental and theoretical research concerning scattering and energy loss processes is largely motivated by a fundamental interest, particularly since experiments can (now) often be readily compared for both electrons and positrons. However, a very important aspect of this research is the need to provide accurate stopping or implantation profiles for monoenergetic positrons, critical for applications such as the near surface studies and depth profiling described in §4.

So far the most detailed investigation of positron stopping profiles in the literature is the Monte Carlo study reported by Valkealahti and Nieminen (1984). This work is presently being extended by Lynn and McKeown (see Schultz and Lynn, 1988, for examples). Fig. 19 shows the end points of 5 keV positrons incident on semi–infinite Al, calculated for 1000 particle histories down to a termination energy of 20 eV. The distribution of positrons versus depth (z) in the sample is well described using a Makhovian function,

$$P(z) = \frac{m z^{m-1}}{z_0{}^m} \exp[-(z/z_0)^m] \qquad (10)$$

where m is an empirically determined shape parameter ($m \approx 1.9$), and z_0 depends on the mean stopping depth, $\bar{z}$,

$$z_0 = \frac{\bar{z}}{\Gamma[(1/m)+1]} \qquad (11)$$

In the above, the Γ function simplifies for certain profiles. For example, if $m=1$, Eq. (10) describes an exponential profile and $\Gamma(2)=1$, and for $m=2$, the profile is a Gaussian derivative and $\Gamma(3/2)=\pi^{1/2}/2$. In practice, using a profile to fit experimental data with a real value for m is computationally excessive, and Vehanen et al. (1987) have shown that $m=2$ is adequate for most purposes. The mean depth is related to incident positron

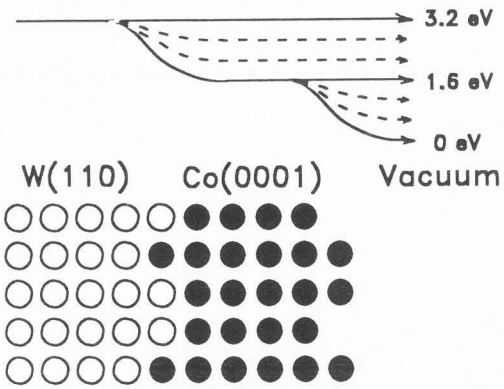

Figure 21: Schematic of Re–emitted Positron Spectroscopy (RPS) for monolayer films of Co(0001) grown on a W(110) substrate. Positrons which are elastically emitted from the buried substrate will have ≈3.2 eV of kinetic energy (the value of the positron workfunction for W(110)), and those which lose *enough* energy to equilibrate in the cobalt overlayer will come out with ≈1.6 eV of kinetic energy. The dashed curves represent inelastically scattered positrons, which can be emitted with any energy between zero and the maximum.

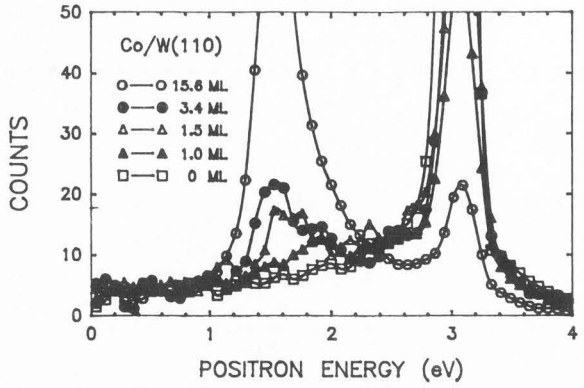

Figure 22: RPS data for the Co/W(110) system (after Ociepa et al., 1990).

energy through a simple power law,

$$\bar{z} = AT^n \tag{12}$$

where z in Å, T in keV, and ρ is the material density [g/cm^3], and the constant A was found empirically to be a $A \approx 400/\rho$ [Å/keV^n]. The power n=1.6 is usually assumed, although Nielsen et al. (1990) have recently shown that for one investigation of bilayered materials the power is better expressed as a function of energy, viz,

$$n = 1.923 - 0.95 \ell n T \tag{13}$$

The mean penetration depth, $\bar{z}$, predicted by the Monte Carlo results for Al is shown in Fig. 20 for both electrons (circle) and positrons (triangle) incident at energies less than 10 keV. Also shown in Fig. 20 are positron data (cross; Mills and Wilson, 1982) and electron data (plus; Vyatskin and Khramov, 1976). This figure illustrates another somewhat suprising prediction: Low energy positrons penetrate *deeper* into the solid than electrons, in spite of the higher cross section for inelastic scattering. This indicates the importance of the elastic scattering cross section (which is larger for electrons) in randomizing the directions before a significant fraction of the energy is lost. Never–the–less, the difference is only a few percent, which indicates that the two effects (larger inelastic cross sections for positrons, and larger elastic cross sections for electrons) cancel each other to *some* extent.

4.0 Applications

After positrons are thermalized in a solid they diffuse for up to ≈2x10^{-10} s, with mean diffusion lengths that are no more than a few thousand angstroms. They can annihilate from freely diffusing states, trap at defects, or reach the surface where they either trap, form positronium (Ps), or are re–emitted into the vacuum as free positrons. These interactions, as well as many others, are used for the various applications of positron–beam techniques to solid–surface studies that are reviewed by Schultz and Lynn (1988). In this section we briefly describe two of these applications.

4.1 Re–emitted positron spectroscopy

Positrons can be re–emitted from solid surfaces which have a negative work function, ϕ^+, which is the energy just outside the solid surface relative to that just inside. Positron and electron work functions both have a surface contribution, due to the dipole layer established by electrons spilling into the vacuum (D), and a bulk contribution, due to the internal energy (usually referred to as the chemical potential, μ). The positron and electron chemical potentials are not related, except as far as the lattice structure and parameters contribute to the zero–point energy. The dipole, on the other hand, is *identical* but of opposite sign for both. The work functions are defined,

$$\begin{aligned} \phi^- &= D - \mu^- \\ \phi^+ &= -D - \mu^+ \end{aligned} \tag{14}$$

and it is the contribution of D, itself several eV, which ensures that ϕ^- is *always* positive whereas ϕ^+ is *often* negative.

Re–emitted Positron Spectroscopy (RPS) contains information about changes in ϕ^+ due to impurity coverage (Gullikson et al., 1988). Energy loss processes at the surface are also revealed in RPS measurements, as demonstrated by studies of the vibrational modes for adsorbed CO on Ni(100) (Fischer et al., 1983). An area now receiving considerable attention is the application of RPS to studies of thin films. In the first study of this type for the Cu/W(110) system (Schultz et al., 1983), it was shown that simultaneous measurements of ϕ^+ and ϕ^- provide separation of surface and bulk contributions to work function changes, which can be extremely useful for investigations of the early stages of thin film growth on a dissimilar substrate. Gidley and Frieze (1988; and Gidley, 1989) have extended this technique, and have shown that transitions from pseudomorphic growth (overlayer constrained to substrate epitaxy) to strain–relieved layers (usually accompanied by dislocations) can be related to the disappearance rate of the characteristic "substrate peak" in the spectrum. This technique is one of a very few available that can *non–destructively* monitor overlayers from below one to a few tens of monolayers (ml).

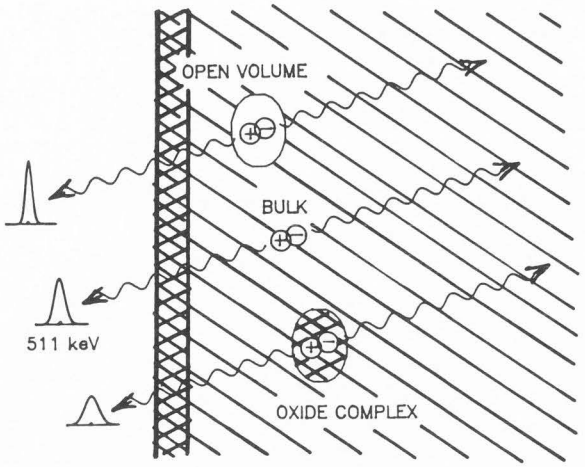

Figure 23: Illustration of Doppler broadening of the annihilation γ–ray from different environments near the surface of a silicon single crystal. Data are characterized by the S–parameter, which is the relative fraction of events in a fixed central portion of the peak. Annihilations from open–volume defects (*e.g.*, vacancies) in Si lead to a *narrower* lineshape (larger S) than for freely diffusing positrons in bulk Si. Annihilations from oxygen–decorated defects, or from the surface oxide, lead to a *broader* lineshape (smaller S) than the bulk value.

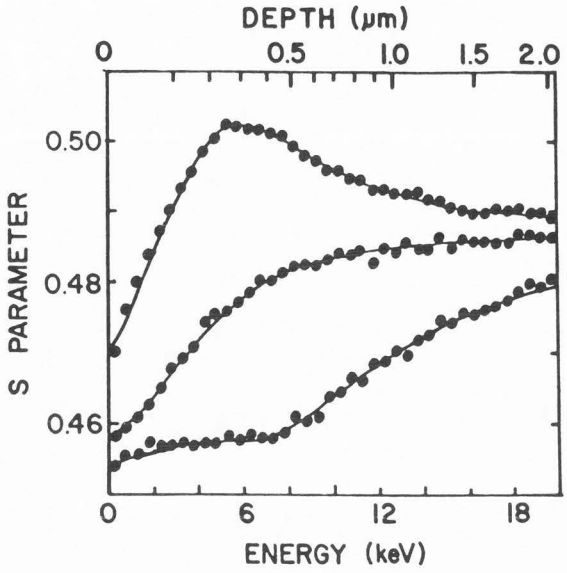

Figure 24: Doppler–broadening lineshape S–parameter is shown versus incident positron energy (or mean stopping depth) in silicon. The middle curve is for bulk, undefected Si(100) as obtained from the manufacturer. The upper and lower curves are for single MBE–grown Si/Si(100) layers, which were 0.3 μm and 0.35 μm thick, respectively. Different substrate prepartations resulted in high concentrations of open–volume defects in the one case (upper), and oxygen–decorated defects in the other (lower).

In Fig. 21 we show a schematic representation of an experiment recently done by Ociepa et al.(1990), to measure the RPS distributions for thin Co layers on a W(110) substrate. Positrons that have thermalized in the W substrate are ≈3.2 volts above the vacuum level, and ≈1.6 volts above their equilibrium energy in Co. Because of the mean free path (Fig. 14) there is a high probability that positrons leaving the W will *not* scatter inelastically in a thin Co overlayer, and so the elastic peak for W is only slowly reduced in intensity by the overlayer. Those that do scatter in the Co layer appear as "inelastics" in between the two elastic peaks, unless they equilibrate in the Co. In this case, they are re–emitted either elastically (≈1.6 volts above the vacuum level), or they lose energy at the surface and contribute to the low energy inelastic tail.

Some of the data from this experiment are shown in Fig. 22, for layers ranging from 0 to 15.6 ml. The figure shows the derivative of data taken using a retarding field analyzer in a magnetically guided positron beam, which measures the normal component, E_z, of re–emitted positron energy. This is referred to simply as "Positron Energy" in Fig. 22. The elastic peak for positrons which thermalize in the Co(0001) overlayer is seen at ≈1.6 eV. The Co peak appears at 1 ml, at which time the hexagonal (2–fold symmetry) Low Energy Electron Diffraction (LEED) pattern for W(110) shows a ≈20% spot splitting in the [110] direction. This indicates that the hexagonal Co overlayer has relaxed to its bulk lattice parameters. During the next 2 ml the LEED spot splitting fades into the characteristic (6–fold) hexagonal pattern of Co(0001), although the positron substrate peak for the W(110) is still observed.

The "zero" of energy occurs at the contact–potential difference between the sample and the grid, $(\phi^- - \phi_g)$, and does *not* move if changes occur in ϕ^+ alone. The W elastic peak is at $(\phi^+ + \phi^- - \phi_g)$, and so changes in this position reflect changes in the sum of the chemical potentials, $-(\mu^- + \mu^+)$, which is related to *bulk* solid properties. Changes in the surface dipole lead to equal and opposite changes in ϕ^- and ϕ^+, which leaves the elastic peak at the same absolute position but causes a shift in the zero. In the data shown in Fig. 22, it can be seen that the W elastic peak did *not* move, which indicates that no significant changes were occuring in the bulk energy levels of positrons and electrons in the W substrate due to the Co overlayer.

One of the most suprising features of the data in Fig. 22 is the observation of an elastic Co peak with just 1 ml coverage. One explanation of this is that more positrons are scattered parallel to the surface, which could allow an observable fraction to equilibrate at the Co potential. The enhanced scattering could result from the 20% mismatch in the lattice parameters of the Co monolayer relative to the W(110) substrate. Another explanation which also involves excessive scattering is that the reconstructed overlayer (which led to the LEED spot splitting) is causing an unusual angular distribution of the re–emitted positrons. Here the total energy would still be that of the W elastic peak (≈3.2 eV), but an enhanced fraction of the re–emitted positrons would have ≈1.6 eV *less* energy than the main elastic peak in the normal (E_z) direction, due to the dipole layer for the Co/vacuum interface. More work on the Co/W(110) system using this and other methods will be required to solve this puzzle.

4.2 Defect profiling spectroscopy

The application of positron–beam techniques that is receiving by far the most *external* attention at this time is the depth–profiling of defects near semiconductor surfaces. There are few techniques of any type which are sensitive to point defects, and even fewer that can claim

to *non–destructively* profile dilute, non–uniform distributions of defects in layers anywhere from a few 10's of angstroms to a few microns in thickness. Positrons are proving that they can not only do just that, but there is some (limited) sensitivity for separating the effects of different defect types.

In spite of these positive features, the technique is only just getting started. This is because there are several difficulties which were not easy to overcome, and many more which are not yet solved (*e.g.*, Tandberg et al., 1989). As is evident from the foregoing discussion, one of the important problems is to *know* the stopping profile, which implies knowledge of the scattering interactions and cross sections. This has so far been adequately handled using the m=2 profile (Eq. (10)), but this kind of monotonic function of depth will not be adequate for studies of heterostructures, where the densities of the constituent materials can be significantly different. Other problems arise from the inadequate knowledge of positron diffusion in an undefected lattice, from the positron–defect interactions, and from the influence of internal electric fields on positron motion. Most of these problems are only slowly being solved through varied and repeated measurements.

There are too many defect–profiling experiments to list, starting with the first (which included no analysis) by Triftshäuser and Kögel (1982) on ion–damaged polycrystalline Ni samples. Progress in interpreting the data involved inclusion of realistic stopping profiles, diffusion and trapping of positrons, and electric–field effects (Lynn et al., 1986; Mäkinen et al., 1986; Schultz et al, 1988b; Tandberg et al., 1989). Results recently published with full analyses include studies of ion–implanted metals (Bentzon et al., 1987) and semiconductors (Keinonen et al., 1988), oxide–semiconductor interfaces (Nielsen et al., 1987), and molecular beam epitaxy (MBE) grown layers of intrinsic (Schultz et al., 1988b) and highly doped (Jackman et al., 1989) semiconductors.

In most defect–profiling experiments, the Doppler–broadened annihilation lineshape (511 keV) is measured as a function of incident positron energy. The width of the line is characterized by the lineshape parameter "S", which is defined as the integral over a fixed central portion of the peak normalized by the total area of the peak. A *narrow* annihilation line yields a *large* value for S. Following thermalization in a semiconductor positrons diffuse until they annihilate from a "free" state in the bulk (parameter S_b), trap in defects from which they eventually annihilate (S_d), or reach the surface where they (usually) annihilate in an oxide–decorated surface trap (S_s). These processes are illustrated schematically in Fig. 23. More details of our analysis and interpretation of the data can be found in the references listed above, as well as the review by Schultz and Lynn (1988).

In Fig. 24 we show results for 3 different Si samples which illustrate the technique. The central curve is the data and fit for a "perfect" Si(100) substrate crystal, which is continuous from S_s to S_b, determined by the diffusion coefficient for positrons in Si. The upper curve in Fig. 24 is for a 0.3 μm layer of Si grown on a sputter–cleaned Si(100) substrate. Prior to growth the substrate was *not* properly annealed, and a high concentration of defects ($C_d \approx 10^{-4}$ per atom) formed throughout the entire overlayer. This concentration was 3 orders of magnitude higher at the interface. Evidence of the defect type is given by the height of the curve, which in this case required $S_d = 1.04 S_b$ to obtain the fit shown. This suggests *open–volume* defects, and results similar to these have been observed in several different specimens prepared in various ways. The data for positrons at incident energies above ≈6 keV correspond to mean stopping depths beyond the interface. The curvature for these data is similar to that for the undefected Si(100) sample, and the asymptotic limit is the same S_b value.

The lower curve in Fig. 24 is the data and fit for a 0.35 μm Si/Si(100) episystem grown in much the same way as the specimen yielding the upper curve. In this case, however, the cleaning procedure was different, and the resulting defect type throughout the overlayer is interpreted as an oxygen–decorated complex (illustrated schematically in Fig. 23). In addition, these data show much more curvature in the undefected substrate (above ≈8 keV) than the central curve. This is due to a bipolar electric field directed towards the interface, caused by active (boron) impurities between the substrate and overlayer. These data were discussed extensively by Schultz et al. (1988b).

The most important result which can be demonstrated by the discussion in this section is the *sensitivity* to (i) different defect types, (ii) depth–dependence of defect concentrations, and (iii) electric–field effects. New problems arise at a much higher rate than experiments can be done, and future goals for studying density mismatched multilayers will be attainable as we improve our understanding of how and where positrons stop in the solid.

5.0 Conclusions

The slowing–down of monoenergetic, low energy (<100 keV) positrons which enter a solid surface has been discussed, emphasizing the differences between positron and electron interactions. The total elastic scattering cross section is larger for electrons than for positrons, which results in larger predicted backscattering coefficients. Experimental data for positron and electron backscattering are not as convincing, and the results of both on–going and future studies will be required to establish the relative fractions. Inelastic scattering cross sections, contrary to elastic, are significantly larger for positrons than for electrons in this energy regime. This inequality has been confirmed by studies of inner–shell ionization, but energy–straggling distributions measured for equivelocity positrons and electrons are still somewhat ambiguous. Finally, stopping profiles for positrons were discussed and two of the many applications of the technique were introduced.

Acknowledgement

The authors gratefully acknowledge many useful discussions and interactions with K.F. Canter, M.G. Cottam, D.W. Gidley, H.H. Jorch, T.E. Jackman, K.G. Lynn, R.M. Nieminen, J.G. Ociepa, E. Tandberg, and A. Vehanen.

References

Ashley JC, Tung CJ, Ritchie RH. (1979). Electron inelastic mean free paths and energy losses in solids. Surf. Sci. 81, 409–426.

Baker JA, Coleman PG. (1988). Measurement of coefficients for the back–scattering of 0.5–30 keV positrons from metallic surfaces. J. Phys. C: Solid State Phys. 21, L875–L880.

Bentzon MD, Huomo H, Vehanen A, Hautojärvi P, Lahtinen J, Hautala, M. (1987). Sputtering damage in Mo(111) studied with slow positrons and computer simulations. J. Phys. F: Met. Phys. 17, 1477–1490.

Bethe HA. (1933). Quantenmechanik der ein– und zwei–elektronenprobleme. Handbuch für Physik, Vol. 24/2, Julius Springer, Berlin, p.273.

Bhabha HJ. (1936). The scattering of positrons by electrons with exchange on Dirac's theory of the positron. Proc. Roy. Soc. (London) A154, 195–206.

Bichsel H. (1990). Energy loss of electrons below 10 keV. Scanning Microscopy Supplement 4., 147-156.

Bishop HE. (1967). Electron scattering in thick targets. Brit. J. Appl. Phys. 18, 703–715.

Cosslett VE, Thomas RN. (1965). Multiple scattering of 5–30 keV electrons in evaporated metal films III: Backscattering and absorption. Brit. J. Appl. Phys. 16, 779–796.

Darlington EH. (1975). Backscattering of 10–100 keV electrons from thick targets. J. Phys. D: Appl. Phys., 8, 85–93.

Drescher H, Reimer L, Seidel H. (1970). Backscattering and secondary–electron emission of 10–100 keV electrons and correlations to scanning electron–microscopy. Z. Angew. Phys. 29, 331–336.

Ebel F, Faust W, Hahn C, Langer S, Rückert M, Schneider H, Singe A, Tobehn I. (1988). Inner shell ionization by electrons and positrons, in: Positron Annihilation, Proceedings of the 8th International Conference, Gent, Belgium, Aug. 29–Sept. 3, 1988, World Scientific Publ., Singapore, 295–296.

Evans RD. (1955). The Atomic Nucleus. McGraw–Hill Book Company, Inc., New York, 594–599.

Fischer DA, Lynn KG, Frieze WE. (1983). Reemitted–positron energy–loss spectroscopy: a novel probe of adsorbate vibrational levels. Phys. Rev. Lett. 50, 1149–1152.

Gidley DW. (1989). Positron tunneling and emission from pseudomorphically grown Ni films on Cu substrates. Phys. Rev. Lett. 62, 811–814.

Gidley DW, Frieze WE. (1988). Reemitted–positron spectroscopy of thin metal films. Phys. Rev. Lett. 60, 1193–1196.

Gryzinski M. (1965). Classical theory of atomic collisions, I: Theory of inelastic collisions. Phys. Rev. A 138, 336–358.

Gullikson EM, Mills AP Jr, Murray CA. (1988). Dependence of the positron reemission probability on the positron work function of a metal surface. Phys. Rev. B 38, 1705–1708.

Hunger H–J, Rogaschewski S. (1986). A study of electron backscattering of thin films on substrates. Scanning 8, 257–263.

ICRU (International Commission on Radiation Units and Measures) (1984). Report No. 37: Stopping powers for electrons and positrons.

Ito S, Shimizu S, Kawaratani T, Kubota K. (1980). Inner–shell ionization of silver by 100–400 keV electrons and positrons. Phys. Rev. A 22, 407–412.

Jackman TE, Aers GC, Denhoff MW, Schultz PJ. (1989). Point defect production in arsenic–doped silicon studied using variable–energy positrons. Appl. Phys. A 49, 335–339.

Jackson JD. (1975). Classical Electrodynamics, Second Edition. John Wiley and Sons, Inc., New York, pp.719–724.

Keinonen J, Hautala M, Rauhala E, Karttunen V, Kuronen A, Räisänen J, Lahtinen J, Vehanen A, Punkka E, Hautojärvi P. (1988). Defect formation in H implantation of crystalline Si. Phys. Rev. B 37, 8269–8277.

Knoll GF. (1979). Radiation detection and measurement. John Wiley and Sons, p.57.

Kolbenstvedt H. (1967). Simple theory for K–ionization by relativistic electrons. J. Appl. Phys. 38, 4785–4787.

Kuzminikh, VA, Pogrebnyak, AD, Vorobiev, SA. (1984). Calculations of positron absorption in targets. Nucl. Instrum. Meth. in Physics Res. B4, 23–33.

Kuzminikh VA, Tsekhanovski IA, Vorobiev SA. (1974). Backscattering of positrons from thick targets. Nucl. Instrum. and Meth. 118, 269–271.

Landau L. (1944). On the energy loss of fast particles by ionization. J. Phys. (U.S.S.R.) 8, 201–205.

Lennard WN, Schultz PJ, Massoumi GR. (1988a). Energy loss distributions for equivelocity positrons and electrons transmitted through a beryllium foil. Nucl. Instrum. Meth. in Physics Research B33, 128–132.

Lennard WN, Schultz PJ, Massoumi GR, Logan LR. (1988b). Observation of the difference between e^-–e^- and e^+–e^- interactions. Phys. Rev. Lett. 61, 2428–2430.

Lindhard J. (1965). The influence of crystal lattice on motion of energetic charged particles. Dan. Vidensk. Selsk. Mat.–Fys. Medd. 34, No. 14.

Logan LR, Cottam MG, Schultz PJ, Jorch HH. (1988). Reflection of positrons from one dimensional crystals, in: Positron Annihilation, Proceedings of the 8th International Conference, Gent, Belgium, Aug. 29–Sept. 3, 1988, World Scientific Publ., Singapore, 300–302.

Lynn KG, Chen DM, Nielsen B, Pareja R, Myers S. (1986). Variable–energy positron–beam studies of Ni implanted with He. Phys. Rev. B 34, 1449–1458.

Mäkinen J, Vehanen A, Hautojärvi P, Huomo H, Lahtinen J, Nieminen RM, Valkealahti S. (1986). Vacancy–type defect distributions near argon sputtered Al(110) surface studied by variable–energy positrons and molecular dynamics simulations. Surf. Sci. 175, 385–414.

Matsukawa T, Shimizu R, Hashimoto H. (1974). Measurements of the energy distribution of backscattered kilovolt electrons with a sperical retarding–field analyser. J. Phys. D: Appl. Phys. 7, 695–702.

Mills AP Jr, Wilson RJ. (1982). Transmission of 1–6 keV positrons through thin metal films. Phys. Rev. A 26, 490–500.

Møller C. (1932). Zur theorie des durchgangs schneller elektronen durch materie. Annalen der Physik 14, 531–585.

Mott NF. (1929). The scattering of fast electrons by atomic nuclei. Proc. Roy. Soc. (London) A124, 426–442; (1932). The polarisation of electrons by double scattering. ibid A135, 429–458.

Nielsen B, Lynn KG, Chen Y–C, Welch DO. (1987). The SiO_2/Si interface probed with a variable–energy positron beam. Appl. Phys. Lett. 51, 1022–1024.

Nielsen B, Van der Kolk GJ, Lynn KG, Leung TC, Van Ijzendoorn LJ. (1990). The range of slow positrons in metal overlayers on Al. Appl. Phys. Lett., in press.

Nieminen RM, Oliva J. (1980). Theory of positronium formation and positron emission at metal surfaces. Phys. Rev. B 22, 2226–2247.

Ociepa JG, Schultz PJ, Griffiths K, Norton PR. (1990). Re–emitted positron spectroscopy from thin Co films on W(110). Surface Science 225 (in press).

Powell CJ. (1976). Cross sections for ionization of inner–shell electrons by electrons. Rev. Mod. Phys. 48, 33–47.

Powell CJ. (1984). Inelastic mean free paths and attenuation lengths of low–energy electrons in solids.

Scanning Electron Micros., 1649–1664.

Rohrlich F, Carlson BC. (1954). Positron–electron differences in energy loss and multiple scattering. Phys. Rev. 93, 38–44.

Schultz PJ. (1988). A variable–energy positron beam for low to medium energy research. Nucl. Instrum. Meth. in Phys. Res. B 30, 94–104.

Schultz PJ, Campbell JL. (1985). Cross–section ratio for K–shell ionization of copper by low energy electrons and positrons. Phys. Lett. 112A, 316–318.

Schultz PJ, Lynn KG. (1988). Interaction of positron beams with surfaces, thin films, and interfaces.Rev. Mod. Phys. 60, 701–779.

Schultz PJ, Lynn KG, Frieze WE, Vehanen A. (1983). Observation of defects associated with the Cu/W(110) interface as studied with variable–energy positrons. Phys. Rev. B 27, 6626–6634.

Schultz PJ, Logan LR, Jackman TE, Davies JA. (1988a). Channeling effects on positron transmission through thin crystals. Phys. Rev. B 38, 6369–6379.

Schultz PJ, Tandberg E, Lynn KG, Nielsen B, Jackman TE, Denhoff MW, Aers GC. (1988b). Defects and impurities at the Si/Si(100) interface studied with monoenergetic positrons. Phys. Rev. Lett. 61, 187–190.

Sigmund P, Winterbon KB. (1974). Small–angle multiple scattering of ions in the screened Coulomb region. Nucl. Instrum. Meth. 119, 541–557.

Tabata T, Ito R, Okabe S. (1971). An empirical equation for the backscattering coefficient of electrons. Nucl. Instrum. Meth. 94, 509–513.

Tandberg E, Schultz PJ, Aers GC, Jackman TE. (1989). Defect profiling of semiconductor epilayers using positron beams. Can. J. Phys. 67, 275–282.

Tougaard S, Sigmund P. (1982). Influence of elastic and inelastic scattering on energy spectra of electrons emitted from solids. Phys. Rev. B 25, 4452–4466.

Triftshäuser W, Kögel G. (1982). Defect structures below the surface in metals investigated by monoenergetic positrons. Phys. Rev. Lett. 48, 1741–1744.

Uehling EA. (1954). Penetration of heavy charged particles in matter. Annual Rev. Nucl. Sci. 4, 315.

Valkealahti S, Nieminen RM. (1984). Monte Carlo calculations of keV electron and positron slowing down in solids, II. Appl. Phys. A 35, 51–59.

Vehanen A, Saarinen K, Hautojärvi P, Huomo H. (1987). Profiling multilayer structures with monoenergetic positrons. Phys. Rev. B 35, 4606–4610.

Vyatskin AY, Trunev VY. (1967). The transmission, reflection and absorption of electrons in thin solid films. Radio Eng. Electron. Phys. 9, 1526–1531.

Vyatskin AY, Khramov VY. (1976). Transmission and absorption of average energy electrons in solid targets. Radio Tek. Electron. Phys. 21, 1931–1935.

Discussion with Reviewers

K. Canter: If one were to look at the energy distribution of backscattering positrons for an incident positron energy of ≈100 keV, would you expect to be able to separate the contributions of multiple small angle scattering from large angle backscattering? It has been suggested by T.C. Griffith and G.R. Heyland that backscattering is better than transmission for producing slow positrons because of enhancement in the β^+ spectrum at low energies due to backscattering via multiple small angle collisions.

Authors: All processes from single, large angle scattering (with low probability) to multiple scattering contribute to the backscattering distribution. Even using the simple continuous slowing down approximation (CSDA) it is clear that this leads to an energy distribution extending from zero up to the primary energy. However, this distribution (which we are now measuring directly) is featureless, with a maximum that is (predictably) not too much below the primary energy. In other words, we do not see any structure which could be ascribed to specific "groups" (see, also, Matsukawa et al., 1974).

As for "slow–positron" beam production, the important point is *where* the positrons stop in the solid, since it is *only* the thermal positrons that are of any value (*i.e.*, $0.1T$ is much too energetic if T>10 keV!) Even though many backscattered positrons are reduced in energy, many more that penetrate into the solid are also energy degraded. For monoenergetic incident positrons, the profile in fact *favors* transmission, since more positrons are stopped at a depth of (for example) 1 μm than at 0.1 μm. For a continuous β spectrum, the profile falls off with penetration depth (favoring back reflection geometry), although it is not a strong function of depth for the first few microns, so there is really not a major advantage to either choice.

K. Canter: Since quantum mechanical exchange effects are negligible above a few hundred eV, the indistinguishability that you say is inherent in Møller's derivation is due to the classical indistinguishability of the electrons. My question is why in the case of inner shell ionization would Møller scattering *not* be appropriate, if one did not choose to observe the resulting x–ray?

Authors: The Møller cross section describes the scattering of two electrons which are initially, and finally, in free particle states. Therefore, a consequence of the quantum–mechanical indistinguishability is that the maximum fractional energy transfer is 1/2. For inner shell ionization, on the other hand, the initial state of the target electron is bound to the atomic nucleus. It is therefore inappropriate to use the Møller cross section to account for the experimental fact that one may observe an ionization event that corresponds to a fractional energy transfer greater than 1/2. A *similar* cross section could, in principle, be derived (as mentioned in the text) which accounts for the binding of the target electron.

R.M. Nieminen: Please clarify the roll of exchange and correlation in the Mott cross section, which is discussed in section 2.

Authors: Our expression for Mott scattering (Eq. (2)) is the McKinley–Feshbach approximation, which is discussed extensively in Evans (1955). It refers to the scattering of electrons or positrons by the static nuclear Coulomb field (charge Ze). It is *not* to be confused with "Mott scattering" of identical particles (*i.e.*, electrons on electrons), which incorporates exchange. The difference in cross sections for e^+ and e^- which is reflected in the last term on the RHS of Eq. (2) arises from the higer order terms of the Born expansion in (αZ), as discussed in section 2 of the text.

At low projectile energies, the atomic nature of the scattering potential also leads to a difference in e^+ and e^- elastic cross sections. In this case, the reason is the larger tail of the scattering potential for electrons due to exchange–correlation effects (Valkealahti and Nieminen, 1984).

R.M. Nieminen: An interesting theme of the work is the comparison between electron and positron scattering properties. Are there simple physical reasons as to why

(i) positrons backscatter less than electrons, and (ii) the elastic scattering (or stopping power) is stronger for positrons?

Authors: There is probably *not* a simple answer to either of these questions. The backscattering difference is simply related to the difference in elastic scattering cross sections for e^+ and e^- (Eq. (2)), as discussed in section 2.1. However, *that* difference is related to quantum mechanical (spin) effects which lead to charge–dependent terms in the second Born approximation of Mott's cross section (section 2). Similarly, the difference in stopping power and other inelastic effects is related to the differences in the Møller and Bhabha cross sections, which are unusually complicated expressions (Eqs. (3) & (5)). In point of fact, the Bhabha cross section is the larger of the two *only* up to 345 keV, above which the Møller cross section is larger!